Sintering regimes and resulting microstructure and properties of binder jet 3D

printed Ni-Mn-Ga magnetic shape memory alloys

Amir Mostafaei, Pierangeli Rodriguez De Vecchis, Erica L. Stevens, Markus Chmielus *

^a Department of Mechanical Engineering and Materials Science, University of Pittsburgh,

Pittsburgh, PA 15261, USA

* Corresponding author: Markus Chmielus

Email addresses: amir.mostafaei@pitt.edu (A. Mostafaei); chmielus@pitt.edu (M.Chmielus)

Abstract

Binder jet printing was used to produce magnetic shape memory foams with densities

increasing from 45% to 99% with increasing sintering temperature from 1000 °C to 1100 °C for 2

h. Within this temperature range, the sintering mechanisms, microstructural evolution, phase

transformation and magnetic behavior were investigated and categorized in three different

sintering regimes. Densification was studied using Archimedes method, optical microscopy and

micro-computed X-ray tomography. X-ray diffraction showed that the pre-alloyed ball-milled

Ni_{49.7}Mn₃₀Ga_{20.3} powder has the austenite phase, however, twinned 14M modulated martensite is

present over the entire sintering temperature range with an increasing formation of martensite

twins with temperature. At the low temperature sintering regime (<1020 °C), solid-state sintering

results in densities of ~45%, consistent composition, phase transformation, Curie temperature and

magnetization. In the medium temperature sintering regime (1020 °C to 1080 °C), solid-state

sintering with grain boundary diffusion happens leading to density up to ~80%. In the high

temperature sintering regime (1090 °C to 1100 °C), liquid phase sintering is dominant leading to

density up to ~99%. In conclusion, binder jet 3D printing of Ni-Mn-Ga alloys show potential to

enable functional elements for complex-shaped applications, and intentional porosity might allow

these polycrystals to exhibit the magnetic field induced strain by reducing constraints between

neighboring grains.

1

Keywords: Additive manufacturing; Ferromagnetic shape memory alloy; Sintering; Porosity; Phase transformation; 14M modulated martensite.

1. Introduction

Ni-Mn-based ferromagnetic alloys have attracted attention due to both the magnetocaloric [1] and magnetic shape memory effects [2]. Based on the composition and microstructure of the magnetic shape memory materials, they can be driven with frequencies up to the kHz regime. In combination with the very large strain and high energy density, this allows for novel applications, which are not feasible using other adaptive materials [3,4]. Ni-Mn-Ga magnetic shape memory alloys (MSMAs) are well-known for showing a magnetic-field-induced strain (MFIS). This MFIS is pseudoplastic and reversible, meaning it is permanent if the magnetic field is removed and can be reversed via an applied perpendicular magnetic field or mechanical stress [5]. The mechanism of MFIS is based on twin boundary motion [6] that results in the reordering of crystallographic domains in an applied magnetic field which lowers magnetization energy [7,8]. The largest MFIS (up to 10%) can be achieved in single crystals when optimally oriented to the magnetic field [6,7]. Polycrystalline bulk Ni-Mn-Ga alloys are not an alternative since neighboring grain are constraining each other resulting in very limited MFIS [9,10]. However, Ni-Mn-Ga single crystals show significant chemical segregation during single crystal growth affecting local composition, crystal structure, and magnetoplastic strain [11].

Two solutions have been proposed to increase the MFIS of polycrystalline Ni-Mn-Ga including (1) increasing porosity to reduce constraints [12] and (2) introducing texture, for instance by directional solidification leading to preferred grain orientation [13]. Boonyongmaneerat et al. [14] showed that introducing pores in polycrystalline Ni-Mn-Ga reduces the internal constraints of grain boundaries to the point that the material displayed a repeatable MFIS of 0.12%. Chmielus

et al. [12] showed the effects of internal and external constraints on MFIS can be reduced by modifying the architecture of the foam with a bimodal pore size distribution, and thereby increase the MFIS to 8.7%. Nilsén et al. [15] used spark plasma sintering to produce Ni-Mn-Ga foam structures and found that the twin movement was facilitated by reduced grain boundary constraints, thus, the measured MFIS of 1.24% was higher than the value reported for coarse-grained Ni-Mn-Ga foams [13]. The main mechanism of reducing internal and external constraints via porosity and foam architecture is based on the reduction of twin-twin and twin-grain boundary interactions [12].

Nevertheless, foam production by replication casting or spark plasma sintering requires the use of strong acids and is time-consuming. In our earlier studies, we investigated binder jet printing (BJP) for structural materials as a fast, low-cost additive manufacturing method which enables complex geometries [16]. Binder jetting is suitable for producing near-net shape parts with controlled porosity, which may be sufficient to overcome grain boundary constraints in polycrystalline Ni-Mn-Ga. The ability to fabricate porous and near net-shape parts with complex geometries could have broad applications in energy applications, lightweight structures, magnets, and sensors [17]. Recently, Caputo and Solomon [18] and Mostafaci et al. [19] reported binder jet printing of Ni-Mn-Ga from pre-alloyed ball-milled powder with angular shape. It was found that parts with green density of ~40% can be binder jet printed and the subsequent sintering may increase density. In our earlier study [19], sintering of the BJP Ni-Mn-Ga part is the most challenging step as oxidation and Mn evaporation may cause compositional and microstructural variations leading to the presence of oxides and different types of martensites such as five-layered (10M), seven-layered (14M) and/or non-modulated (NM) martensite.

Here, we propose a reliable method to produce MSMAs with controlled relative densities from 45% to 99% via binder jet printing and subsequent sintering without oxidation and composition

changes and gradients. Detailed investigations are conducted on the densification, microstructure evolution, thermal and magnetic properties of the BJP and differently sintered samples. The proposed manufacturing process resulted in the formation of structures with microstructural, magnetic and thermal properties similar to the conventionally produced bulk samples.

2. Materials and methods

Ni-Mn-Ga polycrystalline ingots were prepared by induction melting of high purity elements of Ni (99.995%, Kurt J. Lesker), Mn (99.95%, Kurt J. Lesker) and Ga (99.999%, Alfa Aesar) under an argon atmosphere. Ingots with total weight of ~400 g were crushed and ball-milled using a Retsch planetary mill (model PM100) with a speed of 450 rpm for 3 h. Powder with particle size less than 63 μm was obtained by sieving. Figure 1 illustrates an SEM micrograph of the angular Ni-Mn-Ga powder indicating the morphology and size distribution. Chemical composition of the pre-alloyed powder via EDS analysis was Ni_{49.7±0.5}Mn_{30.0±1.0}Ga_{20.3±0.6}.

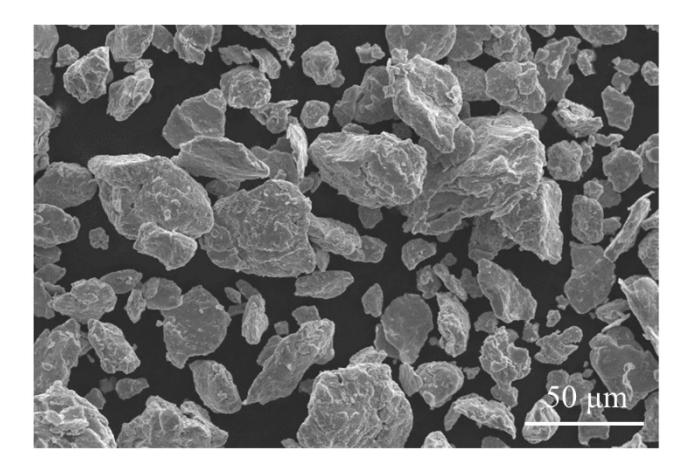


Figure 1. SEM micrograph of the ball-milled pre-alloyed Ni-Mn-Ga powder.

Three types of samples, including cylinders (with diameter of 7 mm and height of 7 mm), rectangular prisms (with dimensions of 3×4×6 mm³) and micro-computed tomography (µCT) samples (diameter of 2.5 mm and height of 5 mm) were printed using an ExOne X1-Lab binder

jet machine with a layer height of 100 μm, spread speed of 20 mm/sec, feed/built powder ratio of 2, drying time of 40 s and binder saturation of 80%. Layers were bound together with an ethylene glycol monomethyl ether and diethylene glycol solvent binder. Titanium sponges (Alfa Aesar, 99.95%) were encapsulated with the samples to prevent oxidation during sintering. To reduce oxygen partial pressure, the capsules were pumped to high vacuum and back-filled with argon gas ten times and finally backfilled with Ar. A Lindberg tube furnace was used for sintering with the following heating profile: heating at 4 °C/min from room temperature to the holding temperature (1000, 1020, 1040, 1060, 1070, 1080, 1090, and 1100 °C), held for 2 h and cooled in air.

Relative density of the sintered samples was measured via the submersion Archimedes method with an OHAUS AX324 precision balance (0.1 mg resolution) as well as from cross-sectional micrographs with the ImageJ image analysis software [20] after taking images using a Nikon Optiphot differential interference contrast (DIC) microscope. For microstructural examination, cross-sections were cut from the cylinder specimens, mounted using epoxy and hardener, then progressively ground and polished to a final step of colloidal acidic alumina using a Struers Tegramin-25 automatic system according to [21]. Besides, density of the sintered CT samples was visualized with a Bruker SkyScan1272 micro-computed tomography scanner (μ CT) with square 2 μ m pixels and 2×2 binning (detailed were summarized in [19]).

Microstructural observation and elemental composition analysis were conducted with a ZEISS Sigma 500 VP scanning electron microscope (SEM) equipped with energy dispersive x-ray spectroscopy (EDS). Phase identification was carried out using an x-ray diffractometer (XRD, Bruker AXS D8 Discover) with Cu–K α radiation (λ = 1.54 Å, 40 kV, 40 mA) with a step of 0.02°, a scan speed of 0.5 sec/step and 2 θ ranging from 35° to 95° at room temperature. The martensitic phase transformation and Curie temperatures were determined from differential scanning

calorimetry (DSC, Perkin Elmer Pyris 6) from 20 °C to 300 °C with heating and cooling rates of 5 °C/min (starting and ending points of plots were cut off at 30 °C and 190 °C). Saturation magnetization at room temperature was measured using vibrating sample magnetometry (Lakeshore model 7407), up to a field of 1.5 T. Thermo-magnetic relations between 30 °C and 130 °C at 50 mT applied field were obtained in an additionally installed Lakeshore model 74034 oven.

3. Results and discussion

3.1. Porosity and relative density measurements

Figure 2 displays the density versus sintering temperature relation of the sintered samples characterized with OM and ImageJ image analysis as well as with Archimedes' method. The results of both methods show similar densification trends as sintering temperatures increased from 1000 °C to 1100 °C. The systematically higher density for samples sintered up to 1080 °C measured via Archimedes compared to OM densities is caused by detaching weakly bonded particles during the grinding and polishing sample preparation step that then appear as pore. Generally, densities at or below ~65% were achieved by sintering between 1000 °C (~50%) and 1070 °C (~65%) which is in agreement with our earlier study on the BJP of Ni-Mn-Ga alloy sintered at 1020 °C [19]. With increasing sintering temperatures from 1070 °C to 1080 °C, a significant increase in relative density to up to ~80% was seen. 1080 °C is close to the solidus temperature of the Ni₅₀Mn₃₀Ga₂₀ composition (reported in [22] which is 1088 °C). Thus, solid state sintering was dominant in the samples sintered from 1000 °C to 1080 °C leading to surface and grain boundary diffusion that resulted in neck formation. However, sintering at 1090 °C and 1100 °C led to densities of ~95% and ~99%, respectively, where liquid phase sintering was dominant. At 1100 °C, samples even partially melted. Therefore, the observed sintering mechanisms seem to be similar to the sintering behavior of Ni-based alloy as shown in [16].

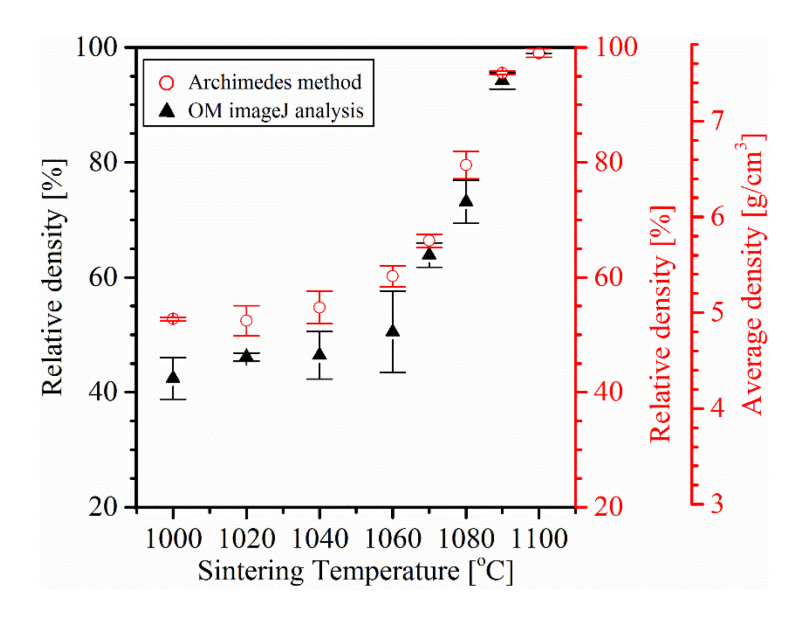


Figure 2. Relative density of the Ni-Mn-Ga BJP samples sintered at the temperatures ranging from 1000 °C to 1100 °C based on the optical micrograph analysis using ImageJ software and Archimedes method.

3.2. Microstructural observations and elemental analyses

The DIC overview of cross-sectional optical micrographs in Figure 3 displays shape, size, and distribution of porosity as well as the microstructure of the sintered Ni-Mn-Ga samples. It was seen that sintering at temperatures from 1000 °C to 1070 °C resulted in samples with mostly connected pores. Since the powder/grain size remained in the same range as the initial powder, solid-state sintering was the active sintering mechanism below 1070 °C. With increasing sintering temperature to 1080 °C, parts with higher relative density were achieved with irregular-shaped pores mainly located at grain boundaries. By increasing the sintering temperature further to 1090 °C, larger and closed round pores formed which is known as pore coarsening [16]. Finally, samples with near-full density were achieved after sintering at 1100 °C.

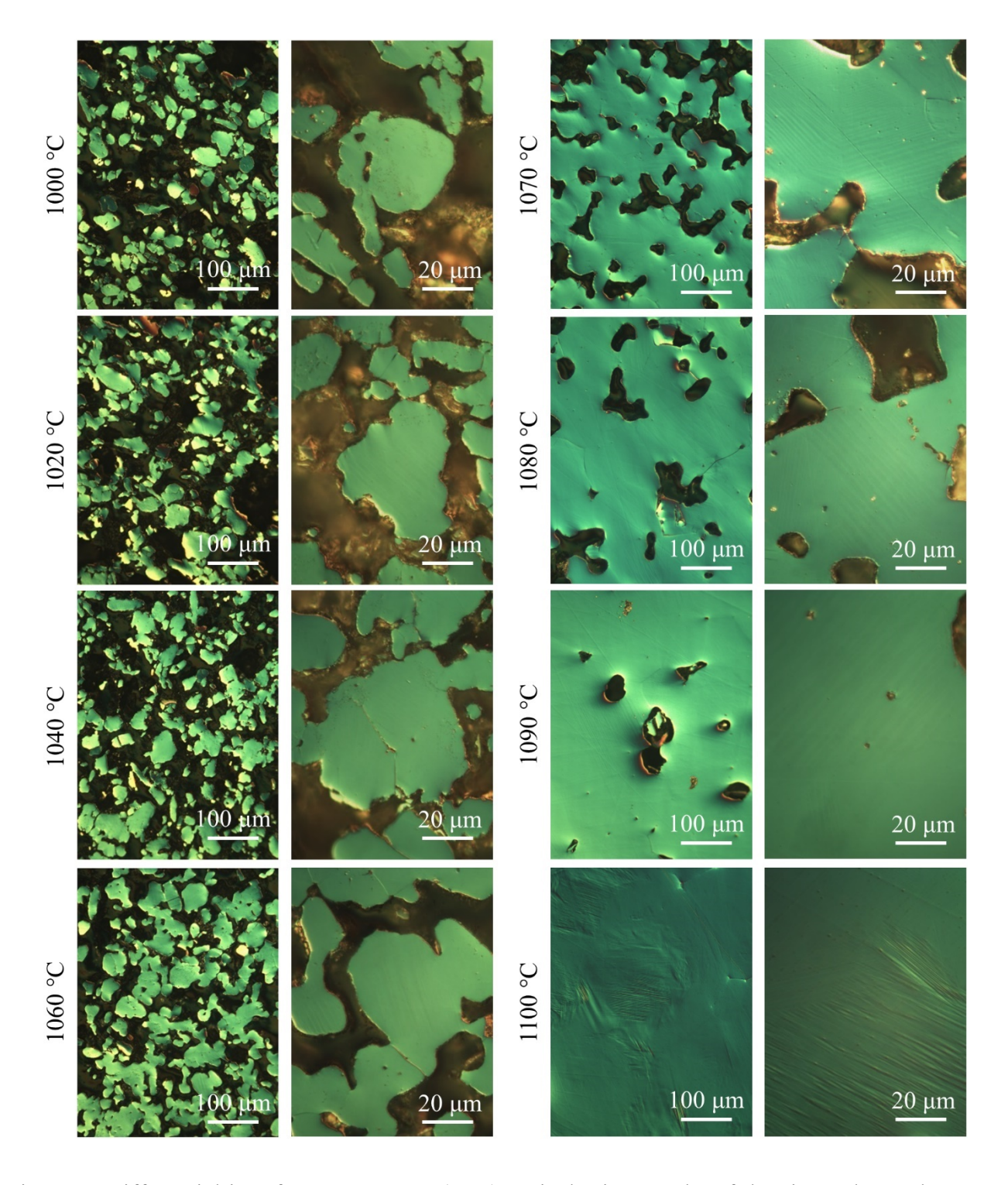


Figure 3. Differential interference contrast (DIC) optical micrographs of the sintered samples at temperatures ranging from 1000 $^{\circ}$ C to 1100 $^{\circ}$ C.

SEM cross-section micrographs of the sintered samples (Figure 4A) show that single powder particles with sharp angular surfaces evolved to round particles with neck formation between them as the sintering temperature increased. For sintering temperatures up to $1060\,^{\circ}$ C, pores were open, connected to each other and mostly irregularly shaped. Sintered At $1080\,^{\circ}$ C, closed pores were seen and pores with round shape were achieved by sintering at $1090\,^{\circ}$ C. It was seen that both the grain size and relative density increased ($150\pm32\,\mu m$ and $\sim99\%$, respectively) with increasing sintering temperature to $1100\,^{\circ}$ C, in agreement with optical observations and density measurements. Martensite twins were observed for all sintering conditions, spanning the width of the grains and terminating at the surfaces of internal pores (porous samples) or at grain boundaries (densified samples). $\sim99\%$ density was achieved for the sample sintered at $1100\,^{\circ}$ C while a Mnrich liquid phase formed at the grain boundaries.

Figure 4B summarized the microstructural evolution during sintering on the surface of the samples. Sintered at 1000 °C, powder particles had sharp and angular edges similar to ball-milled powder particles. With increasing sintering temperature, powder particle became rounder, and short inter-particle necking appeared indicating increased diffusion. For sintering below 1080 °C, bamboo-like grains with triple junctions [23] were visible and sintering above 1080 °C resulted in grain/particle growth and pore reduction. At 1090 °C, liquid phase sintering was dominant leading to pore annihilation. At 1100 °C surface pores were closed. The presence of grains with twins surrounded by pores as well as a bamboo-like microstructure with grains spanning full sections of the metallic necks are necessary for Ni-Mn-Ga to show non-negligible MFIS [14,24].

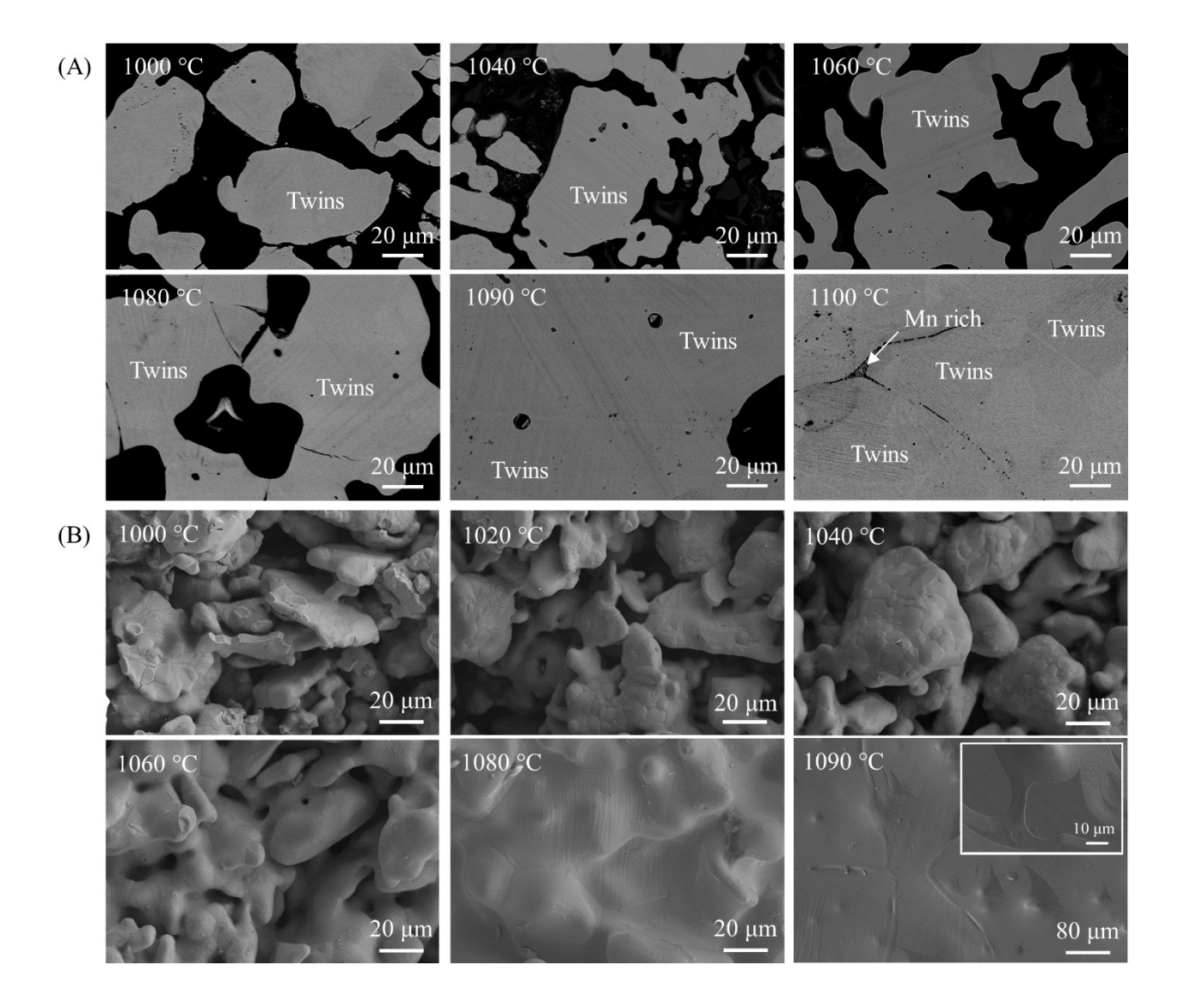


Figure 4. SEM micrographs taken from the cross section of the sintered samples at different temperatures indicating densification process and formation of martensite twins.

Since all properties of magnetic shape memory alloys depend on composition, elemental analysis is a strong indicator of property changes between and within samples [25]. Except for the sample sintered at 1100 °C, compositional EDS analyses (Figure 5 and Table 1) showed a similar composition of around Ni_{50.0}Mn_{29.8}Ga_{20.2} within standard deviation for ball-milled powder and the sintered samples. This indicates that sintering condition did not affect composition, and elemental evaporation (Mn element) was properly controlled during sintering. At 1100 °C, which is clearly

above the solidus temperature, Mn did evaporate and caused a composition change. In a study by Caputo and Solomon [26], a significant difference between powder composition and sintered samples was reported which might have been caused by the used sintering atmosphere and long sintering time. Additionally, here, Ti that was used as oxygen getter during sintering was not detected on any investigated surfaces or cross sections. For the measure composition, Ni-Mn-Ga single crystals should have a 14M martensite as dominant phase [25].

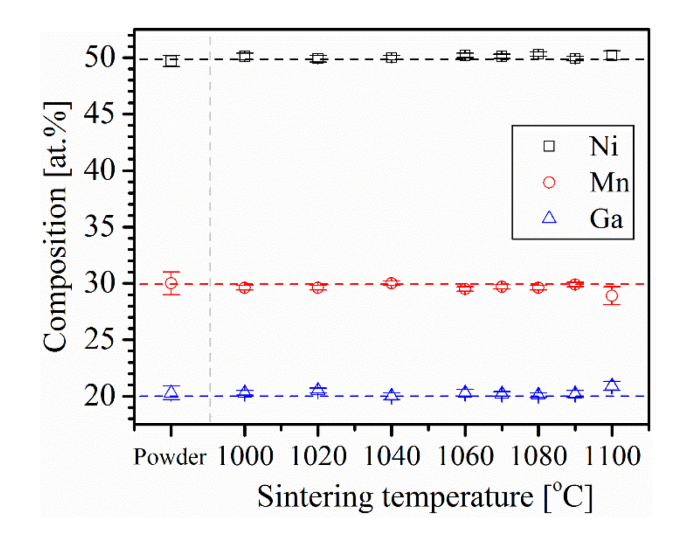


Figure 5. EDS elemental analysis of the Ni-Mn-Ga ball-milled powder and differently sintered samples at temperatures ranging from 1000 °C to 1100 °C. Dash lines indicate the composition of the Ni-Mn-Ga ball-milled powder as reference.

Table 1. EDS elemental analysis and crystallographic parameters for the ball-milled Ni-Mn-Ga powder and differently sintered samples at temperatures ranging from 1000 °C to 1100 °C.

	Ni (at.%)	Mn (at.%)	Ga (at.%)	e/a	а (Å)	<i>b</i> (Å)	c (Å)	Unit-cell volume (ų)	c/b	c/a
Powder	49.7 ± 0.5	30.0 ± 1.0	20.3 ± 0.6	7.680 ± 0.014	5.977	5.977	5.977	213.53	1	1
1000 °C	50.1 ± 0.3	29.6 ± 0.2	20.3 ± 0.2	7.689 ± 0.013	6.153	5.781	5.534	196.85	0.957	0.899
1020 °C	49.9 ± 0.3	29.6 ± 0.2	20.5 ± 0.2	7.676 ± 0.016	6.155	5.785	5.529	196.87	0.956	0.898
1040 °C	50.0 ± 0.2	30.0 ± 0.2	20.0 ± 0.3	7.701 ± 0.009	6.138	5.789	5.536	196.71	0.956	0.902
1060 °C	50.2 ± 0.2	29.5 ± 0.2	20.3 ± 0.3	7.699 ± 0.016	6.135	5.801	5.525	196.63	0.953	0.901
1070 °C	50.1 ± 0.2	29.7 ± 0.2	20.2 ± 0.2	7.687 ± 0.013	6.148	5.787	5.535	196.93	0.957	0.900
1080 °C	50.3 ± 0.2	29.6 ± 0.2	20.1 ± 0.2	7.706 ± 0.014	6.158	5.777	5.524	196.52	0.956	0.897
1090 °C	49.9 ± 0.2	29.9 ± 0.2	20.2 ± 0.3	7.691 ± 0.014	6.142	5.792	5.542	197.15	0.957	0.902
1100 °C	50.2 ± 0.4	28.9 ± 0.8	20.9 ± 0.4	7.667 ± 0.009	6.116	5.810	5.548	197.14	0.955	0.907

3.3. Phase analysis using XRD

The room temperature XRD pattern for the ball-milled Ni-Mn-Ga powder is shown in Figure 6a. The observed peaks were broad and slightly shifted due to the induced stress during ball-milling as reported by Tian et al. [27]. These broad powder peaks at 42.8°, 49.6°, 73.2°, and 88.2° were indexed as (111), (200), (220), and (311), respectively, which corresponds to a disordered cubic austenite phase with calculated lattice parameters of a = b = c = 5.977 Å and the unit-cell volume of 213.5 Å³. During the ball milling process, the mutual collision among the balls, vial wall and the alloy particles resulted in the introduction of lattice distortion, vacancies and other defects to the Ni–Mn–Ga alloy and the atomic order of the Ni–Mn–Ga alloy is destroyed during the process [27]. The lattice distortion from tetragonal to disordered face-centered cubic (fcc) may be reversed upon annealing and sintering at temperatures above 1000 °C [27].

From powder to printed and sintered samples, the XRD patterns change significantly with the introduction of peak splitting and shifts indicating martensite formation (Figure 6a). The martensite modulation of the BJP and sintered Ni-Mn-Ga samples is the most important factor affecting the magnetic anisotropy as well as the mechanical properties of Ni-Mn-Ga ferromagnetic shape memory alloys [28]. Figure 6a and the analyzed results presented in Figure 6b and Table 1 show a change in lattice parameters depending on sintering temperature. The samples sintered between 1000 °C and 1080 °C indicate a dominant 14M martensite while the samples sintered at 1090 °C and 1100 °C show, in addition to the 14M martensite, non-modulated martensite diffraction peaks. The calculated values of lattice parameters indicated that sintering temperatures ranging from 1000 °C to 1090 °C had quite similar a, b and c values. Our calculation (Table 1 and Figure 6c) indicated that the values of lattice parameters are in the order of a > b > c and the lattice distortion ratio c/a for the sintered samples is ranging between 0.897 and 0.907 resulting in a

theoretical maximum MFIS of $\sim 10\%$ (MFIS = 1 - c/a). The c/a ratios clearly indicate a pseudo-orthorhombic phase seven-layered martensite structure (or 14M) [7,29], which is also confirmed by Richard et al. [25] and Sokolovskiy et al. [30] based on the composition of present alloy.

Compared to the used ball-milled powder, narrower and discrete X-ray diffraction peaks were detected in the sintered samples with the calculated unit-cell volume of ~197 Å³. Additional XRD diffraction peaks in the sintered samples were due to the monoclinic distortion indicating the presence of structural modulation as reported by [31].

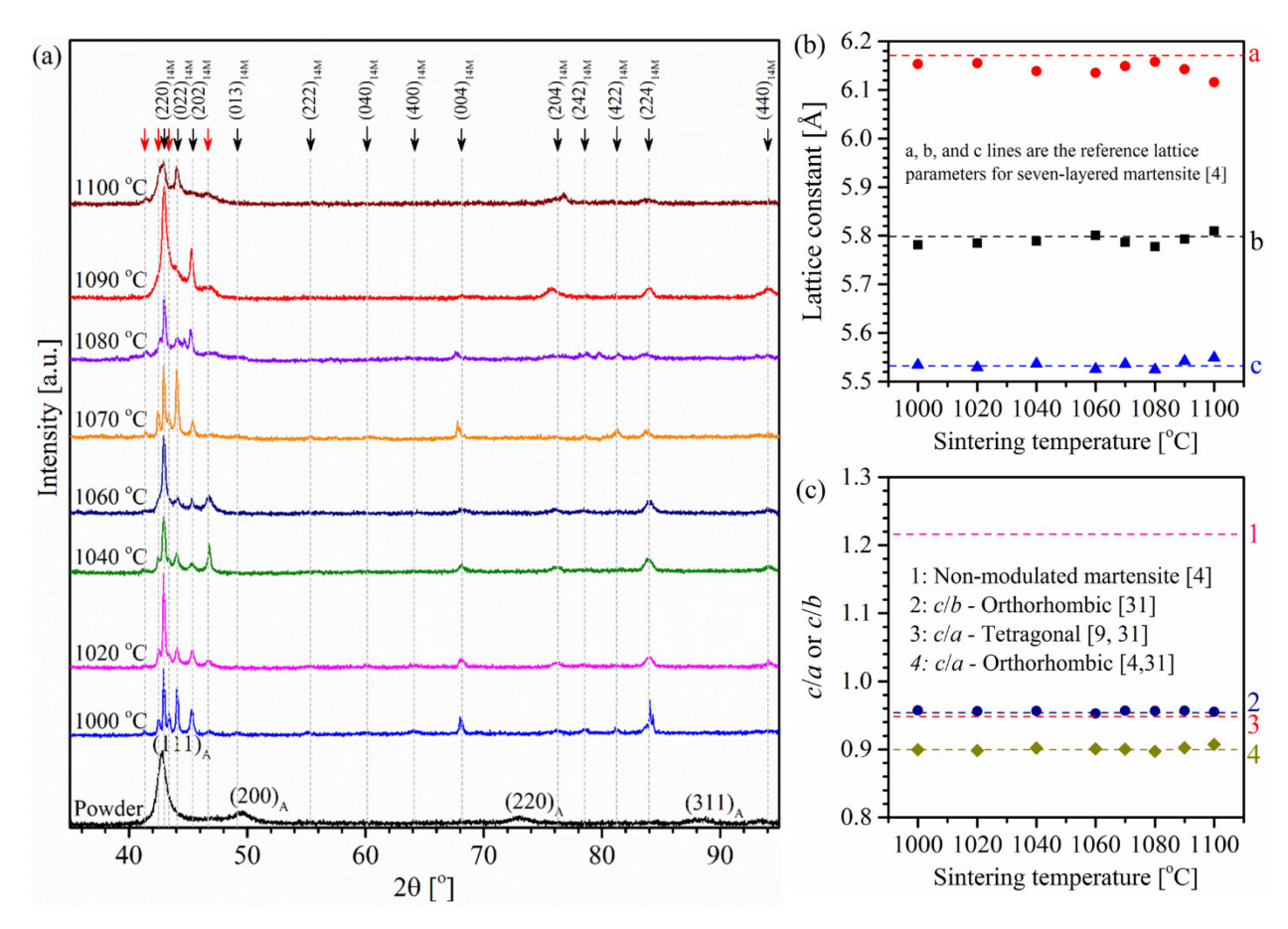


Figure 6. (a) XRD patterns of the ball-milled Ni-Mn-Ga powder and sintered samples at temperatures ranging from 1000 °C to 1100 °C. (b) Crystallographic parameters for the ball-milled Ni-Mn-Ga powder and differently sintered samples. (c) c/a or c/b ratio vs. differently sintered samples. To compare our results with literature, dash lines related to different types of martensites are shown.

3.4. Phase transformation and thermal properties

DSC tests were conducted on the ball-milled powder and all sintered samples (results see Figure 7). The endothermic peak upon heating revealed the transformation from low temperature martensite to a high temperature austenite starting at an onset A_S and ending at A_F . The cooling cycle displays an exothermic peak representing the forward martensitic transformation (austenite to martensite) with a start at M_S and finish at M_F . The characteristic transformation temperatures extracted from the DSC curves are given in Table 2.

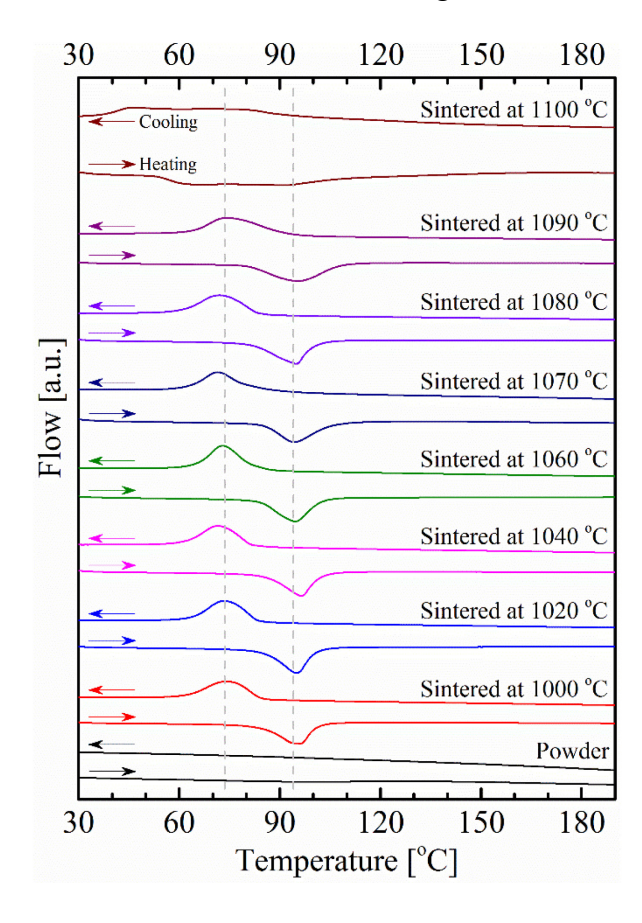


Figure 7. DSC curves of ball-milled Ni-Mn-Ga powder, and sintered samples at different temperatures ranging from 1000 °C to 1100 °C for representing reverse and forward transformations during heating and cooling cycles, respectively.

Table 2. DSC characteristic temperatures and variation in magnetization as a function of temperature for the ball-milled Ni-Mn-Ga powder and differently sintered samples. Calculated magnetic properties obtained from Figure 9 of the ball-milled Ni-Mn-Ga powder, and differently sintered samples.

	<i>A_P</i> (°C)	A _S (°C)	<i>A_F</i> (°C)	<i>M</i> _P (°C)	M _S (°C)	M_F (°C)	T_M (°C)	<i>T_C</i> (°C)	$\begin{array}{c} \Delta H_{M} \rightarrow_{A} \\ (J/g) \end{array}$	$\Delta H_A \rightarrow_M (J/g)$	M_s (Am ² /kg)	H _c (mT)	$\frac{M_r}{(\mathrm{Am^2/kg})}$
Powder	n/a ¹	n/a	n/a	n/a	n/a	n/a	n/a	n/a	n/a	n/a	1.9	0.4	~0
1000	96.1	84.9	101.1	74.3	84.6	63.9	85.2	90	7.25	-7.54	53.9	32.5	7.5
1020	95.1	84.7	101.3	73.6	83.8	63.1	84.4	90	7.70	-7.96	54.2	31.2	7.6
1040	96.4	85.6	102.4	72.6	83.1	62.5	84.5	90	7.35	-7.02	55.8	30.9	8.1
1060	94.6	84.4	102.5	72.9	83.4	63.9	83.8	90	7.89	-8.47	55.7	30.9	7.7
1070	94.4	85.3	103.2	72.5	84.4	63.7	83.5	90	7.20	-7.43	56.5	28.7	6.7
1080	94.9	83.5	101.7	72.1	88.2	62.2	83.5	91	7.92	-8.13	55.6	29.7	6.1
1090	95.5	81.2	108.3	74.7	93.1	62.4	85.1	92	8.72	-8.96	55.5	29.8	6.3
1100	86	57	120	69	42	100	77.5	97	9.78	-10.04	50.1	32.7	8.9

n/a: not available, meaning that the transformation temperatures were not detected during DSC test in the range of 20 °C to 300 °C.

Very broad, barely visible peaks of phase transformation appeared on the DSC curve for the ball-milled powder with the peak broadening attributed again to the atomic disordering caused by ball-milling [27]. However, all sintered samples except for the sample sintered at 1100 °C showed similar behavior as seen in Figure 7 with a clear one-step austenitic transformation upon heating with A_S of ~85 °C, A_F of 102 °C and A_P of 95 °C (A_P is defined as the austenitic transformation peak, ascribed as ($A_S + A_F$)/2). The M_P (known as martensite transformation peak and ascribed as ($M_S + M_F$)/2) was at ~72 °C with the M_S at 84 °C and M_F at 63 °C. Sintering at 1100 °C showed broader phase transformation temperatures for austenite and martensite (values given in Table 2) which might be due to a composition gradient and/or segregation at grain boundaries. The relation between c/a or c/b and M_P was proposed by Lanska *et al.* [7] and would result in our case of c/a ~ 0.9 in a 14M martensite and an M_P of ~73 °C similar to ours. In addition to that correlation, Jin et al.'s [32] proposed relationship between the M_P and valence electrons per atom (e/a) or composition also correlates well.

The span of reverse martensite transformation (A_S-A_F) as well as the forward transformation (M_F-M_S) ranged from 15 °C to 20 °C. Based on Richard et al. [25,33] and our earlier study [19], the Ni-Mn-Ga alloys that are in the pseudo-tetragonal (five-layered martensite or 10M) phase at room temperature show a much sharper transition ($5 \le \Delta T \le 10$ °C) than those which are in pseudoorthorhombic (14M) phase (15 $\leq \Delta T \leq$ 30 °C) in which the terms "sharper" or "broader" refers to the temperature difference between the start and finish of the transition (during heating and cooling cycles). Therefore, the broad peaks in the attained DSC results are also indicative of the pseudoorthorhombic 14M martensite of our samples. The enthalpy (ΔH) values of the BJP and sintered samples were calculated for the reverse and forward phase transformations from the DSC curves and are presented in Table 2. It was seen that the $|\Delta H|$ values were between 7 J/g and 8 J/g for the sintered samples ranging from 1000 °C to 1090 °C in agreement with [34]. Sintering at 1100 °C showed increased $|\Delta H|$ values of 9 J/g and 10 J/g. This again might be attributed to compositional variation in the sample and segregation of a Mn-rich phase at the boundaries (Figure 4A). Second order transformation peaks corresponding to the Curie temperature (T_c) were not visible in the DSC scans, since they overlapped with the first order austenite/martensite transformation peaks as seen in the thermo-magnetic VSM tests performed at 50 mT (see Figure 8 and Table 2).

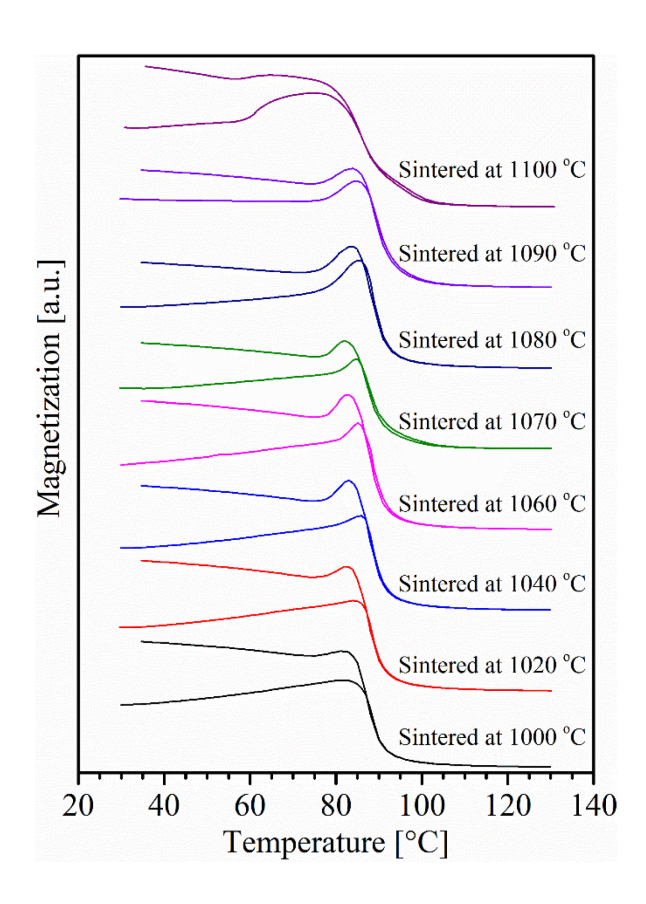


Figure 8. Magnetization vs. temperature curves of the sintered samples at different temperatures ranging from 1000 °C to 1100 °C.

3.5. *Magnetic properties*

The Curie temperatures were determined to be ~90 °C for almost all sintered samples ranging from 1000 °C to 1090 °C. For the specimens sintered at 1100 °C, T_c was slightly higher than the others since melting most likely caused local composition gradients and transformation broadening similar to the effect on the first order transformation. In general, all samples showed the same trend in which the forward transformation from martensite to austenite took place 10-15 °C below T_c at ~90 °C. During cooling, reverse transformation from austenite to martensite took place as shown by the rise of the magnetization. The magnetization slope sign change between the heating and cooling in martensite is typical for a zero field cooling (before the VSM test starts) and then low magnetic field heating and field cooling VSM experiments [35].

The martensitic transformation temperature ($T_M = (M_P + A_P)/2$) values obtained from DSC measurements are given in Table 2. It was found that the T_M values were slightly lower than the T_C values which supports our earlier statement that there might be some overlap between Curie temperature and martensite/austenite phase transformation, similar to Chernenko et al. [36]. However, Martensite phase transformation peaks, M_P in which $M_P = (M_S + M_F)/2$, is lower than the T_C indicates that modulated martensite is present in the structure. Jin et al. [32] presented a contour view of a curve that fitted T_C with experimental data. Based on the EDS analysis results and comparing with [32], the T_C should be ~88 °C which is in agreement with our results. Additionally, an overlap was seen in the phase transformations (T_M and T_C); it was thought that the BJP parts from the used Ni-Mn-Ga material may have potential for the magnetocaloric applications [37–39].

Magnetization hysteresis loops (see Figure 9) of the ball-milled powder and sintered samples were measured at room temperature (25 °C) confirm that all sintered samples showed ferromagnetic behavior at room temperature. The saturation magnetization (M_s), coercivity (H_c) and remnant magnetization (M_r) are summarized in Table 2. It was seen that the differently sintered samples exhibited an M_s of ~56.5 Am²/kg at an applied field of 1.5 T which was significantly higher than the M_s of the ball-milled powder of ~1.9 Am²/kg. It has been known that ball-milling affects magnetization by inducing atomic disorder, changing the Mn-Mn ferromagnetic exchange, which leads to a reduced M_s [35]. Saturation magnetization of ~50 Am²/kg was attained for the BJP sintered sample at 1100 °C which was lower than the other samples and might be attributed to the slight compositional variation as Mn-rich regions formed at the grain boundaries.

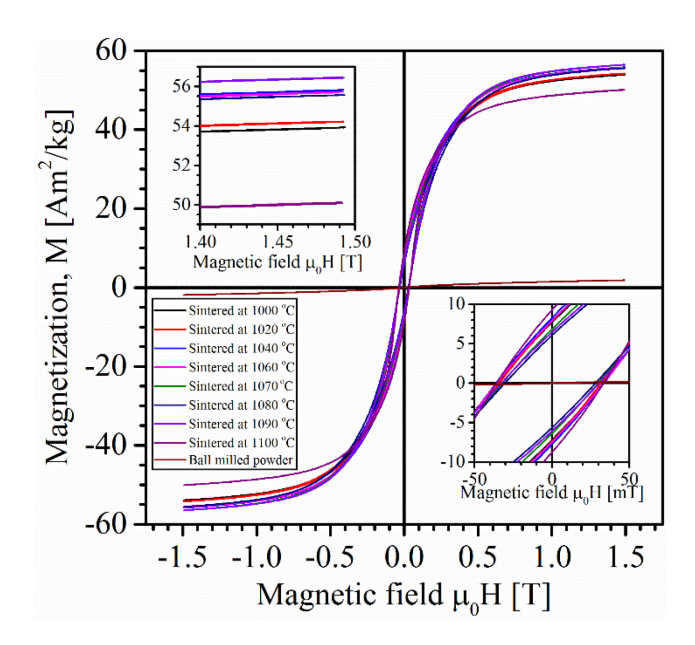


Figure 9. Magnetic hysteresis loops of the ball-milled Ni-Mn-Ga powder, and sintered samples at different temperatures ranging from 1000 °C to 1100 °C.

As reported by Jin et al. [32], saturation magnetization values for different composition of Ni-Mn-Ga alloys were predicted and compared with the measured values by Murray et al. [40] and it was shown that the saturation magnetization may vary between 20 and 60 Am²/kg based on the average number of valence electrons per atom values 7.3 < e/a < 7.8. Heczko et al. [41] and Straka et al. [42] reported the saturation magnetization of ~ 60 Am²/kg for a Ni-Mn-Ga single crystal with seven-layered martensite structure. The difference between the value obtained in this work and [41,42] might be attributed to a slight difference in composition and the potential presence of small volume fractions of non-modulated martensite in sintered samples [10].

4. Sintering mechanism and evolution on microstructure

The sintering process is a critical step in BJ3DP leading to densification of the green part happens through a diffusion at high temperature. While the strength of the green part is due to the polymeric binder added during the printing process and cross-linking during curing, high

mechanical strength can be achieved after sintering with a large controlled variation of final densities and microstructures. Since the green part's density is ~40-50%, the driving force of the sintering is primarily based on the reduction of surface energy. Different regimes during the sintering process affect microstructure and densification behavior summarized in Figure 10. Figure 10a shows the green part prior to sintering. Sinter necks are not present and the surface bonding among powder particles is solely due to the binder. *Initial sintering regime* takes place at lower temperatures where the surface diffusion at contact points of adjacent particles is usually the dominant mass-transport mechanism during the early stages of neck formation [43,44]. Therefore, there is no significant dimensional change or porosity reduction (see Figure 10 b-c). *Intermediate* sintering regime takes place at slightly higher temperatures with grain boundary and volume diffusion being dominant, and parts experience a significant amount of densification up to ~92% as shown in Figure 10d. Additionally, the pores smoothen, become more tubular as opposed to spherical. Subsequently, the pore channels start to close and create isolated porosity via neck growth or the creation of new contact points during pore shrinkage. Thus, material migrates from inside the particles to the surface, resulting in contact flattening and densification. Final sintering regime occurs at the same (with longer holding time) or slightly higher temperatures (with similar or shorter holding time) than the intermediate sintering regime. In the final sintering regime, elimination of the closed pores leads to the maximum possible density. Additionally, solid must be transported into the pores and a means need to exist by which the gas in the pores/voids can migrate to the surface. Very importantly, if the final sintering regime lasts for a long time, elemental segregation and enrichment at the grain boundaries may happen (see Figure 10e). During sintering of Ni-Mn-Ga (this work), parallel lines on the surfaces are indicative of martensite twin

formation within grains. It is worth noting that DIC micrographs with higher magnification showed martensite twin formation in the microstructure in all here sintered samples.

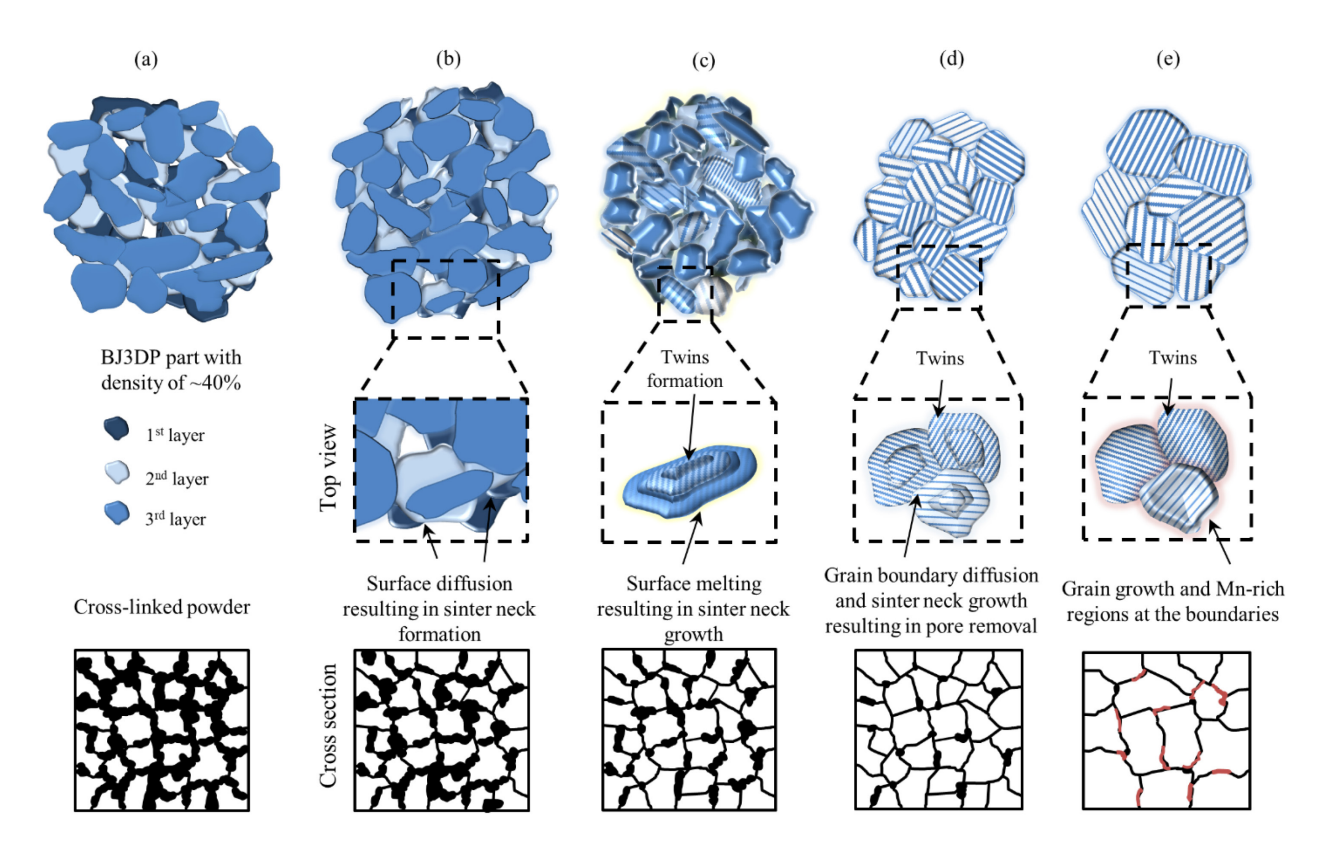


Figure 10. Schematic of different sintering regimes on the BJ3DP from powder particles. (a) cross-linked BJ3DP part indicating loose powder, (b) initial sintering regime where sinter necks form, (c,d) intermediate sintering regime where the density increase due to shrinkage and pores closure, and (e) final sintering regime where the grain coursing happens and prolonging the sintering may lead to elemental enrichment at the grain boundaries. It was seen that twins formed in the grains as the sintered samples and covered entire grain as sintering temperature was increases.

The martensitic crystal structure is correlated to the composition and to some degree to the valence electron concentration (e/a). Non-modulated martensite (NM) tends to have an e/a ratio larger than 7.71, while the modulated martensitic structures (10M or 14M) are associated with an e/a ratio smaller than 7.71 [7,45]. The average e/a ratios were calculated based on EDS compositional analysis for the powder and each sintering condition: e/a was ~7.680 for the ball-milled powder and between 7.68 and 7.70 for the samples sintered at 1000 °C to 1090 °C. The

compositional analysis showed that the sintering temperature of 1100 °C resulted in a slight composition change with a calculated e/a ratio of 7.667. Lanska et al. [7] reported that 14M martensite has an e/a ratio of 7.67-7.71, which agrees with our findings. Generally, the e/a ratio controls to some degree the c/a ratio, phase transformation temperatures (e.g. martensite phase transformation temperature, M_S , Curie temperature, T_C , etc.), saturation magnetization (M_S) and enthalpy (ΔH) values [32,34,40] with each of these discussed above in the related sections.

5. Conclusion

Binder jet 3D printing was used to additively manufacture samples made from angular Ni-Mn-Ga alloy powder and then sintered at temperatures ranging from 1000 °C to 1100 °C for 2 h. The green specimen had a density of ~40% and depending on the applied sintering temperature, solidstate or liquid phase sintering mechanisms dominated the sintering process. It was shown that at the low temperature sintering regime (<1020 °C), solid-state sintering happened leading to density of ~45%. In the medium temperature sintering regime (between 1020 °C to 1080 °C), solid-state sintering with grain boundary diffusion took place resulting in density up to ~80%, consistent composition, phase transformation, Curie temperature and magnetization. In the high temperature sintering regime (1090 °C to 1100 °C), liquid phase sintering was dominant and density increased up to ~99%. Microscopy observations showed that the sinter necks with open pores formed at low sintering temperature and with increasing temperature, grain boundary and volume diffusion led to the densification of the binder jetted part. X-ray diffraction patterns indicated that austenite was present in the ball-milled powder due to residual stress in the ball-milled powder; while 14M martensite was the main phase in the sample sintered from 1000 °C to 1090 °C. Differential scanning calorimetry, thermomagnetic results and vibrating sample magnetometry measurements

showed maximum saturation magnetization of ~56.5 Am²/kg, martensitic transformation temperature of ~73 °C and Curie temperature of ~90 °C by sintering at 1070 °C that resulted in a density of ~66%. Sintering at 1100 °C caused partial melting of the printed part and resulted in the formation of Mn-rich regions at the grain boundaries which might influenced the overall composition of the BJP sintered part and therefore affected phase transformation temperatures and magnetization behavior. Here, we showed a non-beam additive manufacturing method known as binder jetting to produce 3D printed Ni-Mn-Ga alloy with different densities to enable the fabrication of complex-shaped elements for demanding applications, and intentionally including porosity could allow these polycrystals to exhibit the magnetic shape memory effect.

Acknowledgements

Authors would like to acknowledge Dr. Joel Gillespie (director of Materials Characterization Lab (MCL), Dietrich School for Arts and Sciences Shared Research Support Services (SRSS), University of Pittsburgh) for DSC tests, Dr. Volodymyr A. Chernenko for discussions and Jakub Toman, Katerina A. Kimes and Colleen Hilla for their assistance with alloy preparation. The authors would like to acknowledge partial funding from the National Science Foundation [NSF grant number 1727676]. ELS acknowledges funding from the Department of Defense (DoD) through the National Defense Science & Engineering Graduate fellowship (NDSEG) program.

References

- [1] K. Mandal, D. Pal, N. Scheerbaum, J. Lyubina, O. Gutfleisch, Magnetocaloric Effect in Ni Mn Ga Alloys, IEEE Trans. Magn. 44 (2008) 2993–2996.
- [2] S. Dey, S. Singh, R.K. Roy, M. Ghosh, A. Mitra, A.K. Panda, Influence of Mn incorporation for Ni on the magnetocaloric properties of rapidly solidified off-stoichiometric NiMnGa ribbons, J. Magn. Magn. Mater. 397 (2016) 342–346.
- [3] S. Kaufmann, R. Niemann, T. Thersleff, U.K. Róßler, O. Heczko, J. Buschbeck, B. Holzapfel, L. Schultz, S. Fáhler, Modulated martensite: Why it forms and why it deforms easily, New J. Phys. 13 (2011) 53029.
- [4] S. Fähler, Why magnetic shape memory alloys?, Adv. Eng. Mater. 14 (2012) 521–522.
- [5] K. Rolfs, M. Chmielus, R.C. Wimpory, A. Mecklenburg, P. Müllner, R. Schneider, Double twinning in Ni-Mn-Ga-Co, Acta Mater. 58 (2010) 2646–2651.
- [6] N. Zreihan, E. Faran, D. Shilo, The effect of loading rate on characteristics of type II twin boundary motion in Ni-Mn-Ga, Scr. Mater. 144 (2018) 44–47.
- [7] N. Lanska, O. Soderberg, A. Sozinov, Y. Ge, K. Ullakko, V.K. Lindroos, Composition and temperature dependence of the crystal structure of Ni–Mn–Ga alloys, J. Appl. Phys. 95 (2004) 8074–8078.
- [8] K. Ullakko, J.K. Huang, C. Kantner, R.C. O'Handley, V. V Kokorin, J.K. Huang, C. Kantner, V. V Kokorin, Large magnetic-field-induced strains in Ni2MnGa single crystals, Appl. Phys. Lett. 69 (1996) 1966.
- [9] A.K. Panda, S. Singh, R.K. Roy, M. Ghosh, A. Mitra, Effect of Mn incorporation for Ni on the properties of melt spun off-stoichiometric compositions of NiMnGa alloys, J. Magn. Magn. Mater. 323 (2011) 1161–1169.
- [10] O. Söderberg, D. Brown, I. Aaltio, J. Oksanen, J. Syrén, H. Pulkkinen, S.-P. Hannula, Microstructure and properties of Ni–Mn–Ga alloys produced by rapid solidification and pulsed electric current sintering, J. Alloys Compd. 509 (2011) 5981–5987.
- [11] Y. Dai, L. Hou, Y. Fautrelle, Z. Li, C. Esling, Z. Ren, X. Li, Determination of structural and magnetic properties in directionally solidified Ni-Mn-Ga rod with an axial compositional variation, Mater. Des. 134 (2017) 469–475.
- [12] M. Chmielus, X.X. Zhang, C. Witherspoon, D.C. Dunand, P. Müllner, Giant magnetic-field-induced strains in polycrystalline Ni-Mn-Ga foams, Nat. Mater. 8 (2009) 863–866.
- [13] P. Zheng, N.J. Kucza, Z. Wang, P. Müllner, D.C. Dunand, Effect of directional solidification on texture and magnetic-field-induced strain in Ni-Mn-Ga foams with coarse grains, Acta Mater. 86 (2015) 95–101.
- [14] Y. Boonyongmaneerat, M. Chmielus, D. Dunand, P. Müllner, Increasing Magnetoplasticity in Polycrystalline Ni-Mn-Ga by Reducing Internal Constraints through Porosity, Phys. Rev. Lett. 99 (2007) 247201.
- [15] F. Nilsén, J. Lehtonen, Y. Ge, I. Aaltio, S.P. Hannula, Highly porous spark plasma sintered Ni-Mn-Ga structures, Scr. Mater. 139 (2017) 148–151.
- [16] A. Mostafaei, J. Toman, E.L. Stevens, E.T. Hughes, Y.L. Krimer, M. Chmielus, Microstructural evolution and mechanical properties of differently heat-treated binder jet printed samples from gas- and water-atomized alloy 625 powders, Acta Mater. 124 (2017) 280–289.
- [17] L. Li, B. Post, V. Kunc, A.M. Elliott, M.P. Paranthaman, Additive manufacturing of nearnet-shape bonded magnets: Prospects and challenges, Scr. Mater. (2017) 10–14.

- [18] M.P. Caputo, C. V. Solomon, A facile method for producing porous parts with complex geometries from ferromagnetic Ni-Mn-Ga shape memory alloys, Mater. Lett. 200 (2017) 87–89.
- [19] A. Mostafaei, K.A. Kimes, E.L. Stevens, J. Toman, Y.L. Krimer, K. Ullakko, M. Chmielus, Microstructural evolution and magnetic properties of binder jet additive manufactured Ni-Mn-Ga magnetic shape memory alloy foam, Acta Mater. 131 (2017) 482–490.
- [20] C.A. Schneider, W.S. Rasband, K.W. Eliceiri, NIH Image to ImageJ: 25 years of image analysis, Nat. Methods. 9 (2012) 671–675.
- [21] ASM-Standard, Metallography and Microstructures of Nonferrous Alloys, ASM Handb. 9 (2004) 711–751.
- [22] R.W. Overholser, M. Wuttig, D.A. Neumann, Chemical ordering in Ni-Mn-Ga Heusler alloys, Scr. Mater. 40 (1999) 1095–1102.
- [23] M.F. Qian, X.X. Zhang, L.S. Wei, L. Geng, H.X. Peng, Structural, Magnetic and Mechanical Properties of Oligocrystalline Ni-Mn-Ga Shape Memory Microwires, Mater. Today Proc. 2 (2015) S577–S581.
- [24] X.X. Zhang, C. Witherspoon, P. Müllner, D.C. Dunand, Effect of pore architecture on magnetic-field-induced strain in polycrystalline Ni–Mn–Ga, Acta Mater. 59 (2011) 2229–2239.
- [25] M. Richard, J. Feuchtwanger, D. Schlagel, T. Lograsso, S.M. Allen, R.C. O'Handley, Crystal structure and transformation behavior of Ni–Mn–Ga martensites, Scr. Mater. 54 (2006) 1797–1801.
- [26] M. Caputo, C.V. Solomon, Microstructure and Chemical Composition Analysis of Additive Manufactured Ni-Mn-Ga Parts Sintered in Different Conditions, Microsc. Microanal. 23 (2017) 2078–2079.
- [27] B. Tian, F. Chen, Y.X. Tong, L. Li, Y.F. Zheng, Phase Transformation and Magnetic Property of Ni-Mn-Ga Powders Prepared by Dry Ball Milling, J. Mater. Eng. Perform. 21 (2012) 2530–2534.
- [28] A. Sozinov, A.A. Likhachev, N. Lanska, K. Ullakko, Giant magnetic-field-induced strain in NiMnGa seven-layered martensitic phase, Appl. Phys. Lett. 80 (2002) 1746–1748.
- [29] J. Pons, V.A. Chernenko, R. Santamarta, E. Cesari, Crystal structure of martensitic phases in Ni-Mn-Ga shape memory alloys, Acta Mater. 48 (2000) 3027–3038.
- [30] V. Sokolovskiy, A. Grünebohm, V. Buchelnikov, P. Entel, Ab Initio and Monte Carlo Approaches For the MagnetocaloricEffect in Co- and In-Doped Ni-Mn-Ga Heusler Alloys, Entropy. 16 (2014) 4992–5019.
- [31] L. Righi, F. Albertini, E. Villa, A. Paoluzi, G. Calestani, V. Chernenko, S. Besseghini, C. Ritter, F. Passaretti, Crystal structure of 7M modulated Ni-Mn-Ga martensitic phase, Acta Mater. 56 (2008) 4529–4535.
- [32] X. Jin, M. Marioni, D. Bono, S.M. Allen, R.C. O'Handley, T.Y. Hsu, Empirical mapping of Ni-Mn-Ga properties with composition and valence electron concentration, J. Appl. Phys. 91 (2002) 8222–8224.
- [33] M.L. Richard, Systematic analysis of the crystal structure, chemical ordering, and microstructure of Ni–Mn–Ga ferromagnetic shape memory alloys, (2005).
- [34] S.K. Wu, S.T. Yang, Effect of composition on transformation temperatures of Ni-Mn-Ga shape memory alloys, Mater. Lett. 57 (2003) 4291–4296.
- [35] C. Gómez-Polo, J.I. Pérez-Landazábal, V. Recarte, V. Sánchez-Alarcos, G. Badini-Confalonieri, M. Vázquez, Ni-Mn-Ga ferromagnetic shape memory wires, J. Appl. Phys.

- 107 (2010) 123908.
- [36] V. Chernenko, L. Victor, E. Cesari, J. Pons, R. Portier, S. Zagorodnyuk, New Aspects of Structural and Magnetic Behaviour of Martensites in Ni Mn Ga Alloys, Mater. Trans. 43 (2002) 856–860.
- [37] A. Aliev, A. Batdalov, S. Bosko, V. Buchelnikov, I. Dikshtein, V. Khovailo, V. Koledov, R. Levitin, V. Shavrov, T. Takagi, Magnetocaloric effect and magnetization in a Ni-Mn-Ga Heusler alloy in the vicinity of magnetostructural transition, J. Magn. Magn. Mater. 272–276 (2004) 2040–2042.
- [38] V. Basso, C.P. Sasso, K.P. Skokov, O. Gutfleisch, V. V. Khovaylo, Hysteresis and magnetocaloric effect at the magnetostructural phase transition of Ni-Mn-Ga and Ni-Mn-Co-Sn Heusler alloys, Phys. Rev. B Condens. Matter Mater. Phys. 85 (2012) 1–8.
- [39] B. Tian, F. Chen, Y. Liu, Y.F. Zheng, Effect of ball milling and post-annealing on magnetic properties of Ni49.8Mn28.5Ga21.7 alloy powders, Intermetallics. 16 (2008) 1279–1284.
- [40] S.J. Murray, M. Farinelli, C. Kantner, J.K. Huang, S.M. Allen, R.C. O'Handley, Field-induced strain under load in Ni–Mn–Ga magnetic shape memory materials, J. Appl. Phys. 83 (1998) 7297–7299.
- [41] O. Heczko, N. Lanska, O. Soderberg, K. Ullakko, Temperature variation of structure and magnetic properties of Ni-Mn-Ga magnetic shape memory alloys, J. Magn. Magn. Mater. 242–245 (2002) 1446–1449.
- [42] L. Straka, O. Heczko, K. Ullakko, Investigation of magnetic anisotropy of Ni-Mn-Ga seven-layered orthorhombic martensite, J. Magn. Magn. Mater. 272–276 (2004) 2049–2050.
- [43] G.. Kuczynski, The mechanism of densification during sintering of metallic particles, Acta Metall. 4 (1956) 58–61.
- [44] J.G.R. Rockland, The determination of the mechanism of sintering, Acta Metall. 15 (1967) 277–286.
- [45] L. Zhou, M.M. Schneider, A. Giri, K. Cho, Y. Sohn, Microstructural and crystallographic characteristics of modulated martensite, non-modulated martensite, and pre-martensitic tweed austenite in Ni-Mn-Ga alloys, Acta Mater. 134 (2017) 93–103.